



HAL
open science

Development of a compact alpha and beta camera for dismantlement applications

Sylvain Leblond, Pascal Fichet, Laumonier Rémi, Sophie Billon, Paul Sardini,
Kimberly Colas

► **To cite this version:**

Sylvain Leblond, Pascal Fichet, Laumonier Rémi, Sophie Billon, Paul Sardini, et al.. Development of a compact alpha and beta camera for dismantlement applications. *Journal of Radioanalytical and Nuclear Chemistry*, 2022, 331, pp.1075-1089. 10.1007/s10967-021-08172-2 . cea-03939255

HAL Id: cea-03939255

<https://cea.hal.science/cea-03939255v1>

Submitted on 12 Feb 2025

HAL is a multi-disciplinary open access archive for the deposit and dissemination of scientific research documents, whether they are published or not. The documents may come from teaching and research institutions in France or abroad, or from public or private research centers.

L'archive ouverte pluridisciplinaire **HAL**, est destinée au dépôt et à la diffusion de documents scientifiques de niveau recherche, publiés ou non, émanant des établissements d'enseignement et de recherche français ou étrangers, des laboratoires publics ou privés.

1 Development of a compact alpha and beta
2 camera for dismantlement applications

3
4 Sylvain Leblond^{a*}, Pascal Fichet^a, Rémi Laumonier^b, Sophie Billon^c,
5 Paul Sardini^c, Kimberly Colas^a

6
7 ^aUniversité Paris-Saclay, CEA, Service d'Études Analytiques et de Réactivité des Surfaces,
8 91191, Gif-sur-Yvette, France.

9 * curent affiliation : Université Paris-Saclay, CEA, List, Laboratoire National Henri Becquerel (LNE-LNHB), F-
10 91120, Palaiseau, France

11
12 ^bAteliers Laumonier, France

13 Ateliers Laumonier, 11 rue de Chenival - BP 29 - F-95690 Nesles la Vallée, France

14
15 ^cIC2MP, Université de Poitiers, France

16 Université de Poitiers, UMR 7285 CNRS, IC2MP équipe HYDRASA, rue Michel Brunet, Bat. B35, 86073 Poitiers cedex 9,
17 France

18
19 **Abstract**

20
21 A new method has been developed to image surface contamination on-site by short range
22 radiation emitters (such as alpha or beta particle emitters). The measurement is performed in
23 direct contact with the contaminated surface and uses a solid scintillator coupled with Silicon
24 Photomultiplier (SiPM) arrays. The signal readout is processed using a dedicated electronic.
25 The experimental setup used to acquire the data, as well as the analysis procedure, are
26 described and the results are discussed with regard to dismantling requirements. Image
27 reconstruction is investigated using various algorithms. A proof of principle is performed in
28 laboratory using a simple prototype and multiple alpha and beta sources. All the common beta
29 and alpha emitters are detected (including tritium) and tests on gamma radiation are also
30 performed. The minimum detectable activity is estimated to be 0.4 Bq/cm² for beta radiations
31 (¹⁴C) and 0.3 Bq/cm² for alpha radiations (²³⁹Pu). Finally, promising discrimination capability
32 of the prototype is highlighted.

33

34 **Keywords**

35 Dismantling, Autoradiography, Short-range radiation, Contamination imaging

36

37 **Abbreviations**

38 SiPM: Silicon PhotoMultiplier

39 CEA: French Alternative Energies and Atomic Energy Commission

40 ASIC: Application-Specific Integrated Circuit

41 FPGA: Field-Programmable Gate Array

42 ADC: Analog to Digital Converter

43

44

45 **1 Introduction**

46

47 Characterization of radioactive contamination is a mandatory step of any nuclear facility
48 dismantling. It is of first importance to detect, locate, and estimate the nature and activity of
49 the contamination to adapt the dismantling process accordingly [1]. Currently, a large
50 majority of the characterization is performed using destructive radiochemical methods, which
51 require sampling from the facility and offline analysis in a dedicated laboratory [2]. While
52 these methods have good sensitivity, low detection limits, and efficient radioisotopes
53 discrimination, the issue of the sampling representativeness and the required mathematical
54 models to generate and estimated map of the contamination at the scale of the facility are
55 complex issues [3].

56

57 As an alternative, several methods to perform measurements directly on-site have been
58 investigated, most notably for long range radiation [4]. Many projects have developed
59 cameras capable to image directly gamma (see for example [5, 6, 7]) or neutron radiation (see
60 for example [8, 9]). Thus, different industrial solutions are currently available commercially.
61 However, for short-range radiation emitters, such as beta and alpha particles, there is no
62 industrial solution available for dismantling applications, especially for low contamination
63 levels. This issue has been chosen by the international community as one of development
64 needed for the future of contamination characterization [10].

65

66 The main detection difficulty for alpha and beta emitters is related to the high stopping power
67 of radiation in solid matter. This phenomenon comes from the nature and energy of the
68 charged particle emitted during the decay process. On the one hand, the typical energy of the
69 alpha particle encountered in dismantling application ranges from 4 MeV (^{232}Th radiation
70 energy 4.01 MeV) to 7 MeV (^{252}Cf radiation energy 6.12 MeV) [1]. On the other hand, the
71 typical energy range for beta particle is from few keV (^3H mean radiation energy 5.7 keV) to
72 2 MeV (^{90}Y maximum energy 2.28 MeV). The corresponding thickness of plastic required to
73 stop the radiation is thus ranging from 25 μm to 60 μm for the alpha emitters and ranging
74 from few ten of μm to 1 cm for the beta emitters [11]. Thus, few hundred microns of solid
75 matter between the decay location and the sensitive part of any contamination monitor is
76 enough to prevent the detection of short-range emitters. As a consequence, typical
77 contamination monitors used for dismantling application have a limited sensitivity to short
78 range radiations and are not suitable to detect low energy beta particle, such as tritium
79 radiation for example.

80

81 Besides the limited sensitivity, most of the contamination monitors do not provide any
82 information on the localization of the contamination. In practice, the contamination is often
83 assumed to be homogenous at the scale of the sensitive surface of the detector (several tens of
84 cm^2). If such precision is enough to locate a hot spot at the scale of a facility, it can lead to an
85 overproduction of waste during the dismantling process. In addition to the limitation on the
86 precision of the location, traditional contamination monitors are not designed to perform
87 contamination mapping at the facility scale and do not have any storage capability, requiring
88 addition of an external system to reconstruct the map of the contamination.

89

90 To tackle this issue, phosphor screen autoradiography has been used with success to provide a
91 nondestructive but sensitive detection technique capable of imaging short range radiation [12,
92 13, 14]. Yet, the use of phosphor screens is not suitable for further industrial developments for
93 dismantling applications due to the exposure time required which is initially unknown and
94 strongly dependent on the contamination to be investigated. Without any prior knowledge of
95 the type of radiation expected, each measurement requires typically one day. Therefore, a full
96 mapping of a facility is highly time-consuming and quite costly since multiple screens need to

97 be used. In addition, screens are difficult to handle on the field since they require to be
98 handled in dark environment in order to avoid over-exposure [12].

99

100 More recently, several developments have been made [15, 16, 17] to image alpha or beta
101 emitters contamination. All these developments present undeniable progress in specific
102 situation, opening new possibilities for stakeholders dealing with facilities with specific
103 characterizations. However, none of them provide the overall detection capability of the
104 existing contamination monitor, easy to handle, robust for industrial processes and capability
105 of detecting all radiations.

106

107 In this context, the French national radioactive waste management agency (ANDRA) has
108 funded in 2016 a research project to address the mapping of short range emitters
109 contamination. The development aims to provide stakeholders with an efficient way to image
110 surface contamination by short range emitters directly on-site. In this paper, we present the
111 first results obtained with a laboratory prototype and a field demonstrator.

112

113 **2 Laboratory prototype**

114

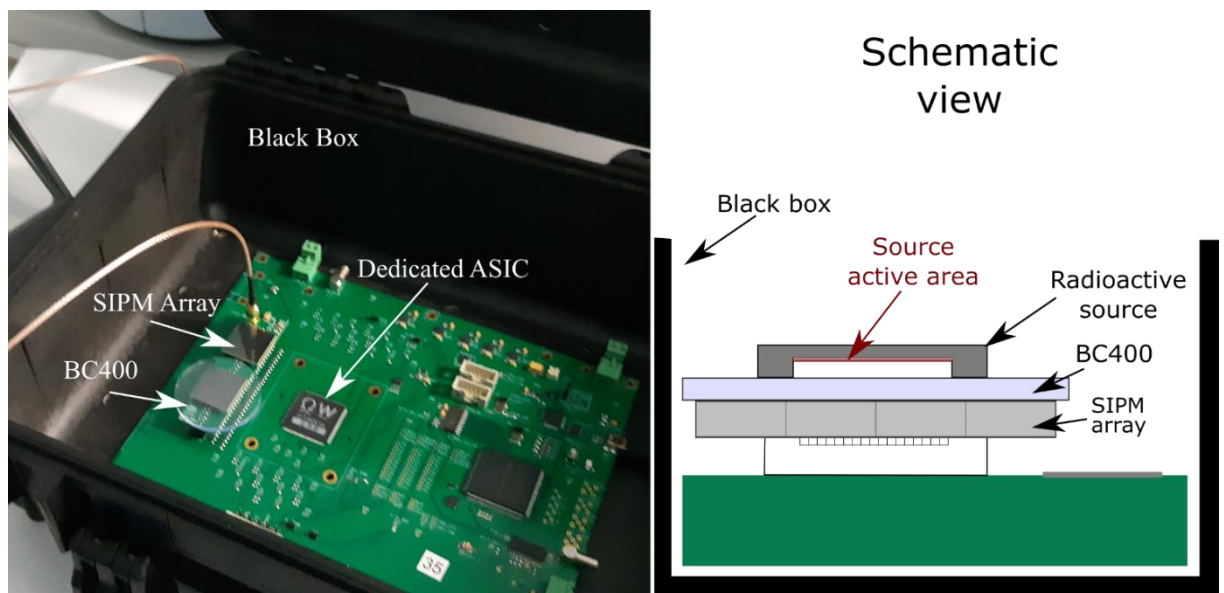
115 In order to obtain high sensitivity when measuring contamination, a prototype with an active
116 detection area in direct contact with the potential contaminated solid surface has been
117 developed. Removing the use of any protective window increases the detection sensitivity,
118 compared to existing contamination monitors, but brings additional constrains. The surfaces
119 encountered in dismantling applications can be dirty, rough or even wet, and require a
120 detector robust enough to be handled in difficult conditions. To meet these requirements, the
121 detection is based on organic scintillators coupled with SiPM arrays, which were used to
122 collect the light emitted when a radiation is going through the scintillator. Organic scintillators
123 are widely used for charged particles detection [18], robust to mechanical constraints and easy
124 to clean. SiPMs provide high gain amplification (typically 10^5 - 10^6), well suited imaging
125 capability with cell size of few mm^2 , and a small form factor (for a portable detector).

126

127 The performance of this detection principle is investigated through experimental tests
128 undertaken in CEA laboratory with a first laboratory prototype. The detection system is based

129 on two independent Hamamatsu S13361-6050 arrays spatially separated by a distance of 21.5
130 mm. On top of each array can be placed a cylindric BC400 plastic scintillator (1 mm thick, 5
131 cm diameter) without any use of optical coupling grease/glue. Each S13361-6050 array is
132 composed of 16 independent cells of individual size of 6 x 6 mm². The readout of the 32
133 channels is performed using a dedicated ASIC, a FPGA and a 12 bits ADC. The prototype
134 was supplied by a Keithley 2450 Sourcemeter® which provides, in addition to the bias
135 voltage, a valuable real time read-out of the current going through the SiPM arrays (typically
136 at the μA level). All the components are enclosed in a hermetic black box to ensure proper
137 light insulation. A picture and a schematic view of the experimental setup are presented in
138 Figure 1. During the experiment, the prototype is connected to a computer using a USB cable
139 and the data acquisition is controlled using a dedicated software developed by the WeeRoc
140 company¹. To insure stable and reproducible conditions for the measurements, the laboratory
141 prototypes are installed in a room with temperature and humidity monitored at 20°C and 40%
142 respectively. It was noticed, however, that the temperature inside the black box was rising at
143 the startup of the measurement due to the heat dissipation of the electronic components. To
144 minimize the effect of temperature, all the measurements presented in the following work are
145 taken 30 mins after turning the system on, after temperature stabilization.

146



147

148 **Figure 1** Left panel is a picture of the first laboratory demonstrator (two SiPM array used, one
149 with BC 400 and one without). The right panel is a schematic view of the same setup (only for
150 the SiPM array covered by the BC400 scintillator).

¹ For more details see <https://www.weeroc.com>

151

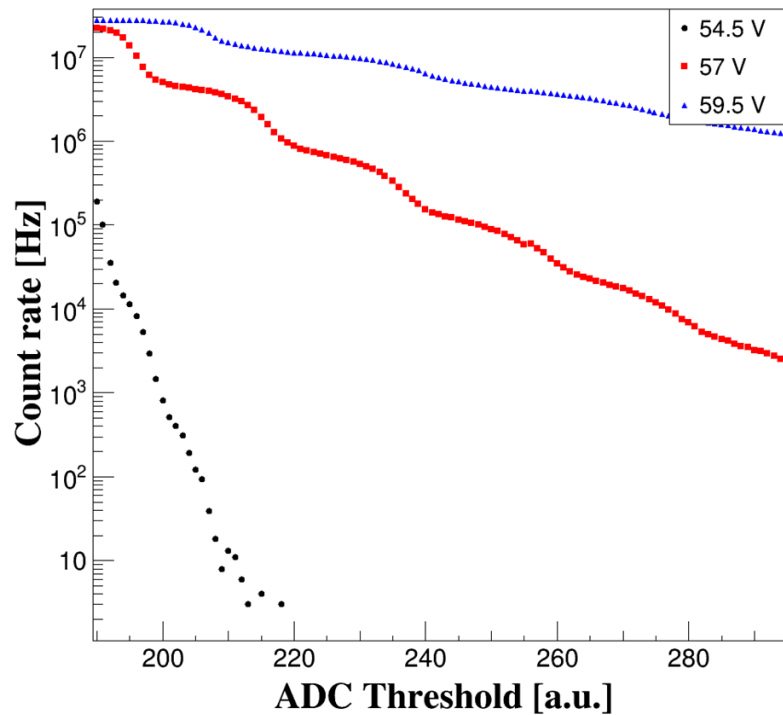
152

153 **3 Prototype operation and calibrations**

154

155 The detection of short-range radiation with the laboratory prototype requires careful
156 adjustment of several parameters. In particular, the SiPM bias voltage is known to have a
157 strong influence over the light amplification gain, the detection efficiency and the internal
158 crosstalk of each SiPM cell (see for example [19]). The detection threshold, i.e. the minimum
159 light intensity which triggers data recording also plays an important role on counting rate and
160 noise reduction.

161 The noise counting rate of the SiPM was studied as a function of the threshold for three
162 different operating voltages. The voltages studied were ranging from the breakdown voltage
163 value provided by the manufacturer and up to an overvoltage of five volts. The results of the
164 study are presented in Figure 2. The measurements were performed without any scintillator or
165 radioactive source, and therefore all detected events were due to the SiPM dark count and
166 optical cross-talk effect. For a given threshold, the noise frequency is rising by several orders
167 of magnitude when increasing the bias voltage. Besides, the noise counting rate is falling
168 much faster, as a function of the threshold value, when decreasing the bias voltage. Since the
169 dark count cannot be distinguished from real photon detection, it is necessary to set a
170 detection threshold high enough to minimize the noise counting rate. However, a detection
171 threshold set too high would strongly lower the detection efficiency of very low energy
172 radiations (which produce a small number of photons in the scintillator). For optimal
173 performance, the prototype could therefore be adjusted for each type of radiation and energy.
174 For simplicity purposes however, a single setting has been used to record the data used in this
175 study. All the measurements have been performed using a fixed operating voltage equal to 55
176 V and a detection threshold corresponding to an equivalent of 12 photons. This relatively low
177 overvoltage, compared to the 54.5 V breakdown voltage, was chosen in order to maximize the
178 detection of low energy radiation, such as beta particle coming from tritium. When the
179 amplitude signal of any of the 32 SiPM (two arrays of 16 SiPM each, see Figure 1) exceeds
180 the detection threshold, data acquisition triggers and the computer records the corresponding
181 Analog to Digital Converter (ADC) value of all the 32 SiPMs cells.



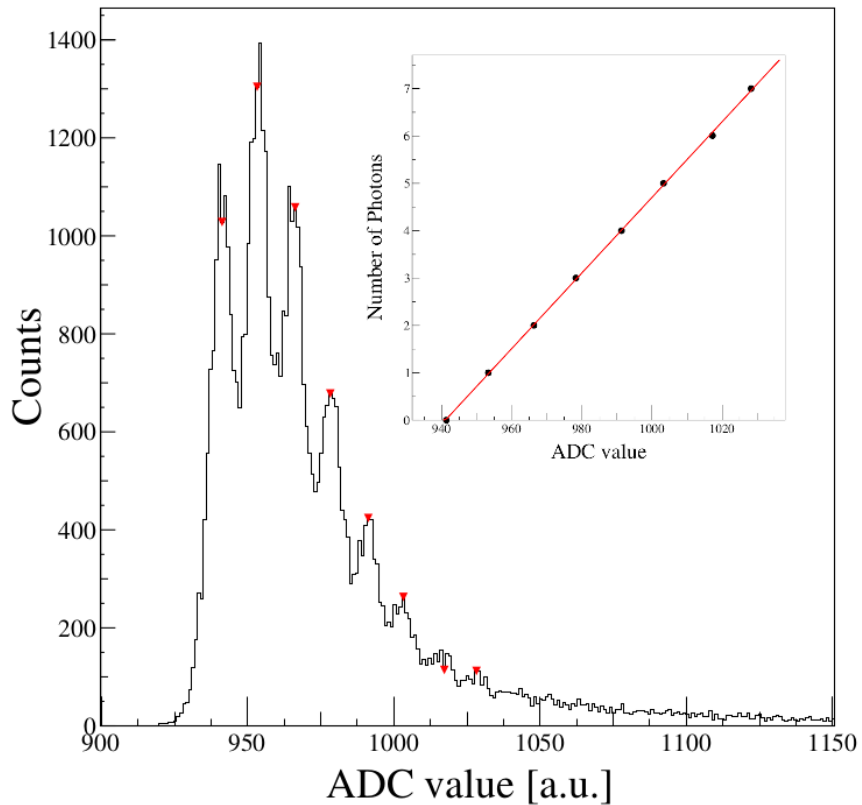
182
183
184
185
186

Figure 2 Evolution of the dark count rate (in Hz) of the prototype as a function of the detection threshold (in arbitrary unit). The study was realized with three different voltages applied to the SiPM: 54.5V (black points), 57V (red squares) and 59.5V (blue triangles).

187 An SiPM provides an analog output signal with amplitude proportional to the number of
188 electric discharges occurring within the cell. For low and intermediate light intensity this
189 discharge number is proportional to the number of incident photons on the SiPM. For one
190 event, it is therefore possible to calibrate the light intensity in a number of photons detected
191 using the numerical value provided by the ADC through the dedicated ASIC. Each SiPM cell
192 of the prototype is calibrated using a ¹⁴C source, a one millimeter thick BC 400 scintillator
193 and a 10 minutes data acquisition. An example of a raw ADC distribution reconstructed for
194 one cell is presented in Figure 3. The position of each peaks, tagged with red triangles,
195 corresponds to an equivalent number of detected photons. Such positions have been estimated
196 using a gaussian fit. From these positions, the calibration of the ADC value into an equivalent
197 number of photons can be performed, using a linear trend and assuming that the first peak
198 corresponds to one photon equivalent (see insert in Figure 3).
199 Based on the calibration of all the SiPM cells of the system, the total light intensity detected
200 by the prototype can be reconstructed event by event:

$$L = \sum_i l_i = \sum_i a_i ADC_i + b_i$$

201 where l_i is the value of the calibrated light intensity, calculated from the ADC_i value,
 202 corresponding to the SiPM index i (from 1 to 32) where a_i and b_i are respectively the slope
 203 and the intercept of the linear calibration.



204
 205 **Figure 3** Distribution of ADC values measured for one SiPM cell of the prototype. The
 206 calibration of ADC value in photon equivalent is shown on top right as an insert.

207
 208 **4 Detection characterization**

209 The detection capability of the laboratory prototype is characterized next using the alpha and
 210 beta sources presented in Table 1.

211
 212
 213
 214

215
216

Table 1 Properties of the various calibrated alpha and beta sources used for the detector characterization.

Isotope	Radiation emission	Mean radiation energy (keV)	Active surface (mm ²)	Emerging (α/β) 2π Activity (Bq)	Surface 2π Activity (Bq/cm ²)
³ H	β	5.7	105	4202 \pm 630	4020
¹⁴ C	β	49.5	1963	1641 \pm 12	84
³⁶ Cl	β	251	908	1634 \pm 12	180
⁹⁰ Sr/ ⁹⁰ Y	β	196 / 934	2640	1627 \pm 12	62
²³⁹ Pu	α (+ β + χ)	5139	177	161 \pm 3	92
²⁴¹ Am	α (+ β + χ + γ)	5364	177	121 \pm 2	68
¹³⁷ Cs	γ + β	662	2640	178 \pm 10	7

217

218 All these radioisotopes are commonly encountered in dismantling applications and were
219 chosen to cover a wide range of energy. These sources are laboratory standards, commonly
220 used for calibration purposes, and therefore have a radiation flux certified by the
221 manufacturer. In addition, the active areas of the sources are thin surfaces in order to
222 minimize attenuation of the radiation energy inside the source material. Finally, the activities
223 of the sources were low enough for manual handling and suited to probe the sensitivity of the
224 prototype at a low level of contamination. In the specific case of the tritium source, only a
225 mass activity (in Bq/cm³) was certified by the manufacturer. However, the apparent activity,
226 i.e. number of particles going out of the sample by time unit, was required to study the
227 prototype response to radiations. Thus, the apparent activity of the source was estimated
228 taking into consideration the attenuation of the radiation in the source material using the
229 GEANT4 simulation described in [20, 21]. In addition to the alpha and beta sources, one
230 gamma source (¹³⁷Cs), was selected to evaluate roughly the response of the prototype to
231 gamma ray emission. Since the ¹³⁷Cs source was unsealed, the beta particles emitted by the
232 decay were stopped using a 1mm thick aluminum foil. The resulting gamma flux was
233 calculated assuming the known branching ratio of the decay and the attenuation of gamma
234 rays in the aluminum.

235 During each individual measurement, the alpha and beta sources are put in direct contact with
236 the scintillator which is placed on top of one SiPM array (see Figure 1 schematic). The
237 acquisition duration is set to 5 minutes which is a reasonable value for on-site measurement of
238 facilities being dismantled.

239

240 4.1 Background measurement

241

242 The background level of the prototype is estimated by performing twelve independent
243 acquisitions over six nonconsecutive days without the use of any radioactive source. For each
244 of the acquisition, the number of recorded events above the acquisition threshold is
245 determined. Over all the acquisitions, the number of events spanned from 141 to 301 counts.
246 The counting rate average is used in the following analyses as the typical background level.
247 The uncertainty on the background counts is estimated, with a 95% confidence level, using
248 Student's t-distribution [22]. The background level is thus equal to 235 ± 35 counts for an
249 acquisition of 5 minutes. This corresponds to a relative uncertainty on the background level
250 around 15%. This represents approximately 0.8 ± 0.1 counts per second for a real time
251 measurement or, taking into account the prototype detection surface, 0.14 ± 0.02 cps/cm².

252

253 From the background average and associated uncertainty, the Detection Limit of the system
254 can be estimated, using the Currie formula [23]:

$$DL = \frac{-b + \sqrt{b^2 + 4ac}}{2a}$$

255 with

$$a = 1$$

$$b = -(2k_{1-\alpha}\sigma_0 + k_{1-\beta}^2)$$

$$c = (k_{1-\alpha}^2 - k_{1-\beta}^2)\sigma_0^2$$

256 for which

$$\sigma_0 = \sqrt{\mu_{BCK} + \sigma_{BCK}}$$

257 Where μ_{BCK} is the background level and σ_{BCK} the associated uncertainty. Additionally, α and β
258 are the expected error probably of false positive counting, respectively false negative

259 counting. Finally, $k_{1-\alpha}$ and $k_{1-\beta}$ are the $1-\alpha$, respectively $1-\beta$, confidence limit interval of the
 260 normal distribution. By taking a false positive and a false negative probability both equal to
 261 5%, the formula can be simplified to:

$$DL = -b + |b|$$

262 The results of the calculation give a detection limit equal to 259 counts for a 5 minutes
 263 acquisition which corresponds to 0.86 count per second for a real time measurement. Taking
 264 into account the prototype detection surface, the detection limit is estimated to be equal to
 265 0.17 cps/cm².

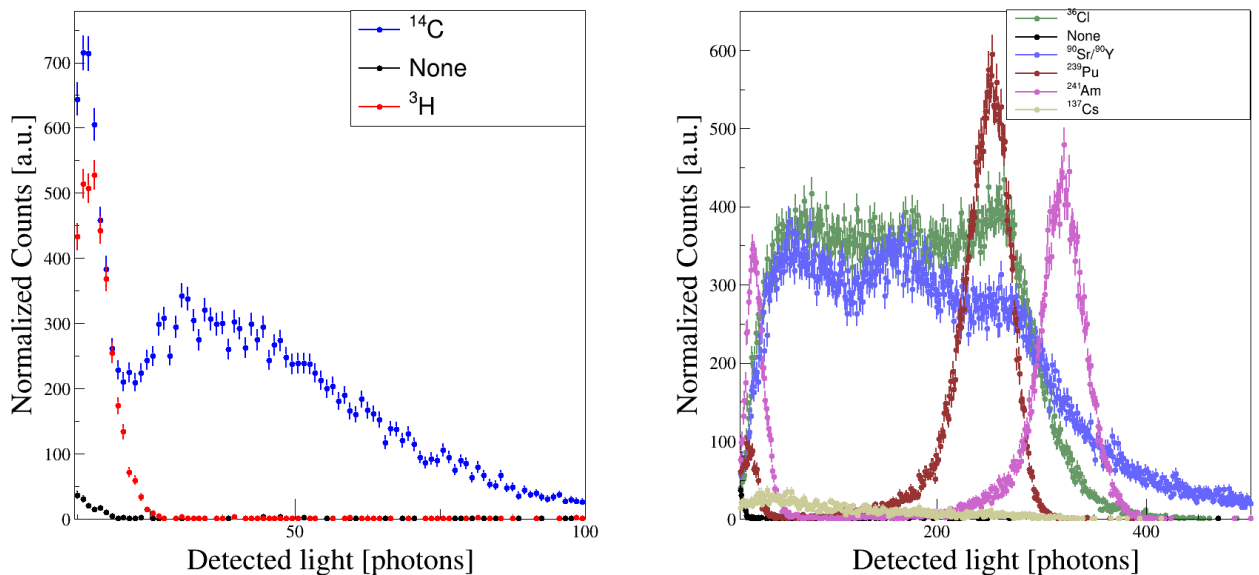
266

267 4.2 Isotope discrimination

268

269 Discrimination of the radiation can be performed using the total calibrated light intensity. The
 270 distributions obtained with each of the sources were compared to background measurements
 271 (performed without any radiation source). The integral of each distribution has been
 272 normalized by the emerging activity of the source. The results are presented in Figure 4.

273



274

275 **Figure 4** Reconstructed light distribution obtained for the radioactive sources. The left panel
 276 shows the light distribution obtained for ³H (red) and ¹⁴C (blue), while the right panel shows
 277 the light distribution for ³⁶Cl (green), ⁹⁰Sr (dark blue), ²³⁹Pu (dark red), ²⁴¹Am (purple), and
 278 ¹³⁷Cs (light grey). In both cases the distribution obtained without any radiation source is
 279 plotted in black.

280

281 A clear distinction between the alpha and beta sources used can be observed. First, the two
282 radiation types exhibit characteristic differences in the reconstructed distribution: the beta
283 spectra are large and continuous while the alpha spectra are characterized by narrow peaks.
284 Secondly, all the sources could be distinguished from each other based on statistical properties
285 of the distributions (such as the average and the standard deviation as display in Table 2). The
286 higher the beta particle energy, the higher the number of detected photons (as expected from
287 energy loss of the radiation in the organic scintillator [24]). A similar result can be observed
288 for the alpha sources, the average number of photons detected for the ^{241}Am being higher than
289 the one measured for the ^{239}Pu source. This result is very promising in the perspective of
290 identifying alpha and beta radiations (more generally performing radiation discrimination)
291 with the demonstrator planned to be tested in the future on the field. However, it should be
292 emphasized that these preliminary measurements have been performed in laboratory with
293 chemically pure sources. In addition, the sources are thin and not affected by the potential
294 matrix effect that could be observed for on-site applications (see for example [20, 21]). To
295 confirm this preliminary discrimination capability, further analysis has to be performed on
296 actual samples and on-site.

297 **Table 2** Number of detected events for a five minutes acquisition, using alpha and beta
298 sources of various activities. The statistical estimators were determined from the distribution
299 measured for each source.

Isotope	Normalized number of events	Light intensity (photons)	Average light intensity per event (photons)	Light intensity standard deviation (photons)
None	235	$1.56 \cdot 10^4$	59	72
^3H	3731	$8.27 \cdot 10^4$	22	34
^{14}C	37141	$7.47 \cdot 10^5$	42	25
^{36}Cl	102046	$1.71 \cdot 10^7$	168	84
$^{90}\text{Sr}/^{90}\text{Y}$	99336	$1.95 \cdot 10^7$	196	120
^{239}Pu	32724	$7.59 \cdot 10^6$	232	55
^{241}Am	31282	$7.82 \cdot 10^6$	250	122
^{137}Cs	3668	$4.19 \cdot 10^5$	114	79

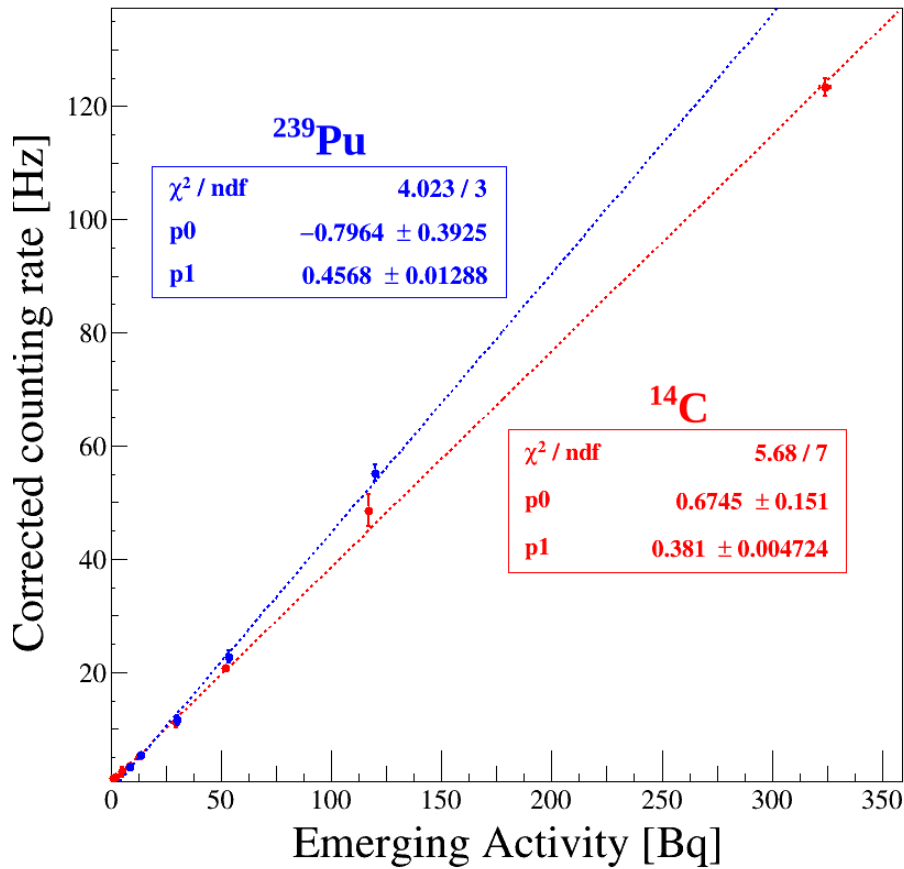
300

301

302 4.3 Detection response linearity

303

304 The counting rate is investigated as a function of source activities by inserting 3 mm thick
305 plastic collimators between the sources and the plastic scintillator. The study was performed
306 with ^{14}C source and ^{239}Pu source, both presenting homogeneous surface contamination. The
307 diameters of the collimator aperture were ranging from 1.1 mm to 25 mm. While all nine
308 different collimators could be used with the ^{14}C source, only five of them were used with the
309 ^{239}Pu due to the source size limitation. For each diameter, the expected detection rate was
310 estimated (see Table 3) assuming homogenous contamination of the source and taking into
311 account the radiation attenuation between the source and the scintillator. The measurements
312 were performed three times for each source and collimator and the average counting rate
313 detected, subtracted from the background counting rate, was determined. The uncertainty on
314 the counting rate was estimated using the standard deviation of the three measurements and
315 Student's t-distribution with a confidence interval of 95%. The results obtained are presented
316 in Figure 5 and in Table 3.



317
318
319
320
321

Figure 5 Study of counting rate of the prototype as function of emerging activity of ^{14}C (in red) and ^{239}Pu (in blue) source. The dashed lines are linear fit of the data points. The parameters of the fit are displayed in the insert boxes (p1 is the slope, p0 the intercept)

322
323
324
325
326
327
328
329
330
331

The data points are fit using linear regression. The coefficients of determination are respectively $R^2 = 0.999$ for the ^{14}C and $R^2 = 0.998$ for the ^{239}Pu . For ^{14}C , the linearity is well verified for all the range of activity, except below 8 Hz of detected events for which the prototype overestimates the emerging activity. For the ^{239}Pu the linearity is verified over all the considered activities. Both for alpha and beta emitter, the detection response is linear enough to perform real time contamination estimation with the field demonstrator to be developed. Due to the low radiation flux coming from the sources, no dead time is observed on the counting rate. Additional studies with higher source activities will be required to investigate further such effect.

332 **Table 3** Expected and measured counting rates for a 5 minutes acquisition, using both ^{14}C and
 333 ^{239}Pu sources. The values are presented for various diameters in the masks used to reduce the
 334 radiation flux.

Hole diameter (mm)	Expected ^{14}C events rate (Hz)	Measured ^{14}C events rate (Hz)	Expected ^{239}Pu events rate (Hz)	Measured ^{239}Pu events rate (Hz)
1.1	0.6	1.2 ± 0.4	-	-
2	2.1	1.5 ± 0.2	-	-
3	4.7	2.4 ± 0.9	-	-
4	8.3	3.4 ± 0.3	11.5	8.5 ± 0.4
5	13.0	5.3 ± 0.7	17.9	13.3 ± 0.7
7.5	29.2	11.3 ± 1	40.3	29.9 ± 0.9
10	51.9	20.7 ± 0.4	71.6	53.2 ± 1.1
15	116.7	48.5 ± 2.9	161.0	119.6 ± 1.5
25	324.1	123.4 ± 1.6	-	-

335

336

337 4.4 Detection efficiency

338

339 The 2π detection efficiency ϵ_R is an important parameter to quantify the prototype sensitivity
 340 to alpha and beta radiations. In particular, a high detection efficiency is to obtain the lowest
 341 possible detection limit. The efficiency of the prototype is estimated using the following
 342 equation:

$$\epsilon_R = \frac{N - \mu_{BCK}}{\tau A_R} F_R$$

343 where N is the number of counts measured during the acquisition time, μ_{BCK} is the
 344 corresponding background level, τ is the acquisition time, A_R the 2π source activity, and F_R a
 345 correction factor to estimate the radiation loss. The latter parameter was introduced in the
 346 equation to take into account the radiation attenuation in air located between the source and
 347 the scintillator. While the source and the scintillator are in close contact (as in Figure 1), a
 348 little space can still generally be observed between the scintillator and the source (except for
 349 tritium) due to the supporting frame thickness (typically around 1 millimeter). The attenuation
 350 in the air between the two layers is calculated based on a GEANT4 simulation above-

351 mentioned [20, 21]. The efficiency of the prototype is calculated for ^{14}C , ^{239}Pu , ^3H and ^{137}Cs
 352 source. Taking advantage of the previous measurements, the efficiency for ^{14}C and ^{239}Pu is
 353 determined by plotting the counting rate as a function of the emerging activity (reported in
 354 Table 3). The slope coefficient of the adjusted data, as well as the associated uncertainty,
 355 provides the detection efficiency for the ^{14}C and ^{239}Pu . Regarding ^3H and ^{137}Cs sources, using
 356 a similar method was not possible. For tritium, the collimator would have needed to be very
 357 thin to keep a reasonable activity (the radiation flux being strongly affected by air). Besides,
 358 the relatively small active area (105 mm²) of the source would have required small holes in
 359 this thin collimator constraining even more the design and construction of such collimator.
 360 Regarding the ^{137}Cs , the gamma radiation could have been collimated using lead but the
 361 connector used between the PCB card and the SiPM arrays can not withstand such heavy
 362 load. Instead, a crude estimation is performed for both sources using a simple procedure.
 363 Three independent measurements are recorded and the average of the observed number of
 364 detected events is compared to the source activity to calculate the efficiency. The uncertainty
 365 on the results is estimated using the standard deviation and Student's t-distribution with a
 366 confidence interval of 95%. The results obtained for all the sources are presented in Table 4.

367 **Table 4** Detection efficiency and minimum detectable activity measured with the radioactive
 368 sources.

Isotope	Radiation	Detection efficiency (%)	Minimum detectable activity (Bq/cm ²)
^3H	B	0.15 ± 0.05	92
^{14}C	B	38.1 ± 0.4	0.36
^{239}Pu	A	45.7 ± 1.3	0.30
^{137}Cs	Γ	6 ± 1.3	2

369

370 As a comparison, two industrial contamination portable monitors (commonly used in nuclear
 371 facilities) are considered: the LB-124 SCINT Series from Berthold technologies [25] and the
 372 NUHP CoMo-170 from NuviaTech Instruments [26]. According to the manufacturer
 373 documentations, the typical efficiency is between 14-29% for ^{14}C and 20 – 45% for ^{239}Pu . The

374 deduced efficiencies obtained with the laboratory prototype are comparable to these industrial
375 references, thus proving the validity of the detection principle for dismantling applications.
376 In the cases of ^3H and ^{137}Cs , the various experimental constrains and assumptions (performed
377 to calculate the emerging activity) are likely to have a high impact on the deduced efficiency.
378 In particular, the estimations of the uncertainty presented in Table 4 only include the statistical
379 uncertainty but no systemic bias. As a consequence, caution should be taken before drawing
380 conclusions from these estimations. Yet, based on the order of magnitude of the efficiency
381 deduced for both nuclei, preliminary observations can be made. On the one hand, it can be
382 stressed out that these first results are very encouraging for tritium measurements for which
383 no industrial solution can be currently found. On the other hand, the gamma detection
384 efficiency of the prototype seems smaller than the one of the above-mentioned portable
385 monitors. Since the detection was optimized for short range radiations (with a thin organic
386 scintillator), this low efficiency was expected and is not a major flaw. Additionally, a small
387 gamma detection efficiency might provide the possibility to study alpha / beta contamination
388 in facilities with high ambient gamma radiation background.

389

390 4.5 Minimum Detectable Activity

391

392 Using the previously deduced efficiency, a refined version of the detection limit can be
393 proposed to include the prototype response to the alpha and beta radiations. The estimation is
394 performed for each source using the following formula:

$$395 \quad MDA_R(\tau) = \frac{DL}{\tau \epsilon_R}$$

396 where DL is the detection limit calculated in the section 4.1, τ is the acquisition time
397 considered, and ϵ_R is the detection efficiency for the radiation considered. The results obtained
398 with the formula are reported in Table 4. For a typical nuclear facility and for safety purposes,
399 a reasonable threshold used to classify a surface as contaminated is 4 Bq/cm^2 for beta/gamma
400 emitters, 0.4 Bq/cm^2 for alpha and 100 Bq/cm^2 for tritium [27]. The minimum detectable
401 activity obtained with the prototype are of the same order of magnitude for an instantaneous
402 measurement, thus confirming the capability of the prototype to meet the dismantlement
403 requirements.

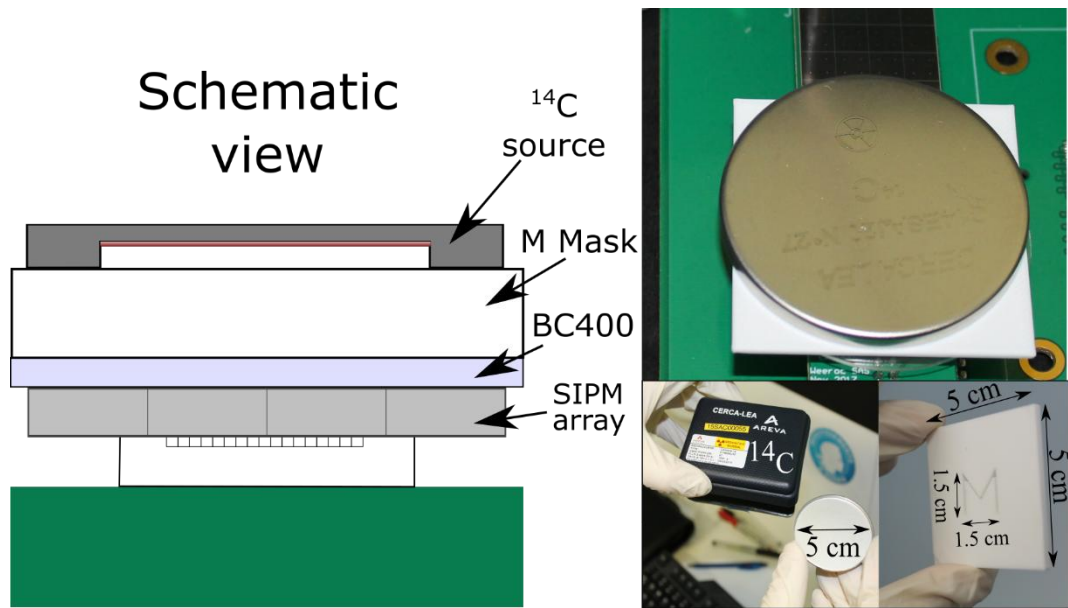
404

405 **5 Image reconstruction**

406

407 Special care has been taken to investigate the image reconstruction capability of the
408 laboratory prototype. A specific collimator was designed with the letter M carved on it (see
409 right bottom panel in Figure 6). The size of the M letter in the collimator was 1.5 cm wide by
410 1.5cm height and the width of the aperture was 1 mm. The collimator is inserted between the
411 ^{14}C source and the scintillator (the associated emerging activity was estimated to be around 43
412 Bq). A one-hour acquisition is performed with this configuration using a detection threshold
413 of 12 photons equivalent for the acquisition. Since the collimator and source are located on
414 the top of one of the two arrays, only this array was considered for the image reconstruction
415 (4x4 SiPM array). Two simple algorithms were developed and compared for the
416 reconstruction of the spatial image of contamination.

417



418

419

420 **Figure 6** The left panel is a schematic view of the setup used to investigate shape
421 reconstruction of the laboratory prototype. The top right panel is a picture of the setup in
422 operation and the bottom panels, picture of the ^{14}C source as well as the M-shape mask.

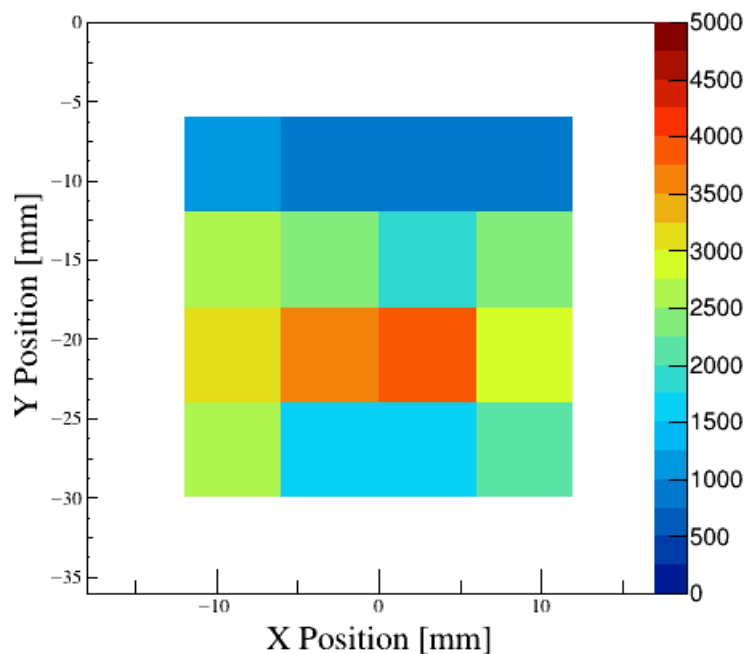
423

424 **5.1 Direct image reconstruction**

425

426 The first algorithm, named *triggering cell algorithm*, is based on the number of hardware
427 trigger occurrences for each SiPM cell. Since these triggers are generated by the dedicated

428 ASIC chip, they are already contained in the data flux from the system which makes the
429 algorithm easy to implement and to run in real time. From the individual values recorded for
430 the 16 cells of the prototype, a 2D image of the contamination is reconstructed. The image
431 displays in a color scale the number of occurrences for each cell as a function of the
432 horizontal (X) and vertical (Y) positions. In this representation, the size of the pixels
433 corresponds to the geometrical size of the individual SiPM cell (6x6 mm²). The result
434 obtained with this algorithm is presented in Figure 7. The color scale (in arbitrary unit) is
435 chosen to enhance the image contrast. The image obtained shows clear counting variation
436 from a pixel to another, ranging from 607 to 3972 counts. This wide range of registered
437 triggers corresponds to the variation of the emerging radiation flux on the investigated
438 surface. However, due to the size of the pixels, the shape of the letter M can barely be
439 distinguished and the obtained shape looks closer to a H capital letter.



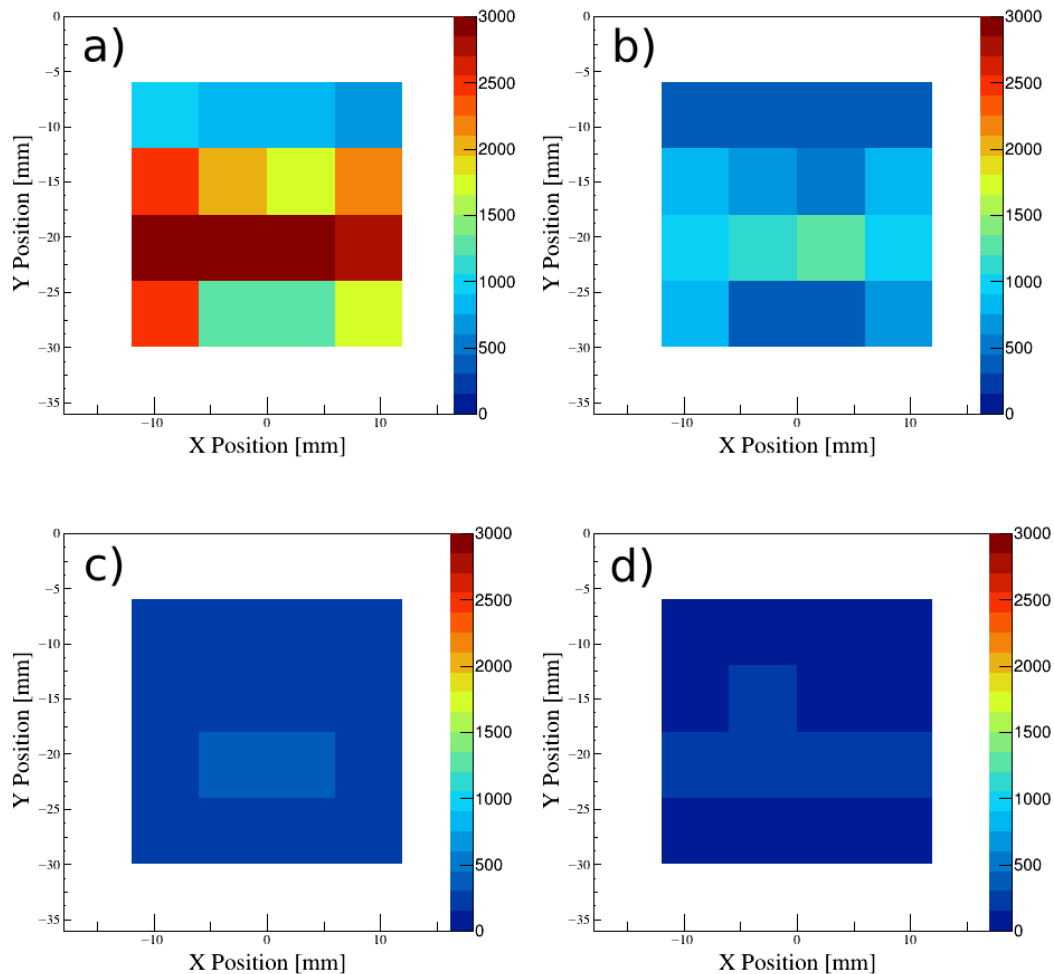
440

441 **Figure 7** Spatial reconstruction of the emerging radiation flux of ¹⁴C through a M-shaped
442 collimator using the *triggering cell algorithm*

443

444 The influence of the threshold value on the image quality is investigated by performing the
445 reconstruction with different thresholds: 12 equivalent photons, 25 equivalent photons, 50
446 equivalent photons and 100 equivalent photons. The results obtained are presented in Figure

447 8. The shape of the letter can be distinguished with low light intensity thresholds but vanished
448 and become homogenous at higher thresholds. As mentioned previously, the light intensity by
449 the prototype depends on the energy but also the type of the radiation. Thus, the image
450 reconstruction with *triggering cell algorithm* has to be optimized for each type of source.
451 Such optimization is not discussed in the present article since only the overall behavior of the
452 prototype is discussed.



453
454
455
456
457

Figure 8 Spatial reconstruction of radioactive contamination of ^{14}C source after a M collimator with the *triggering cell algorithm*. The four panels correspond to different thresholds: a) to 12 photons, b) to 25 photons c) to 50 photons and d) to 100 photons

458 5.2 Refined image reconstruction

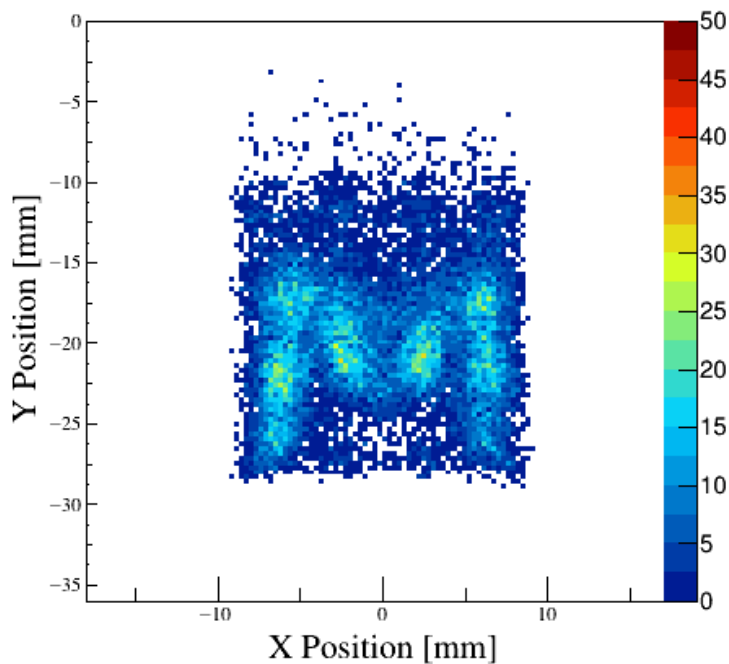
459

460 A third algorithm, named *weighted average algorithm*, was developed based on the properties
461 of the organic scintillator. Since the light is emitted isotropically by the BC400 scintillator

462 along the radiation path, the light intensity detected by each cell should be directly
 463 proportional to its geometrical acceptance. Thus, one can have a good approximation of
 464 emission position by analyzing the light distribution registered by each cell. For each event,
 465 the emission position is reconstructed by performing the following weighted average:

$$X_{event} = \sum_i X_i \frac{l_i}{L} \quad Y_{event} = \sum_i Y_i \frac{l_i}{L}$$

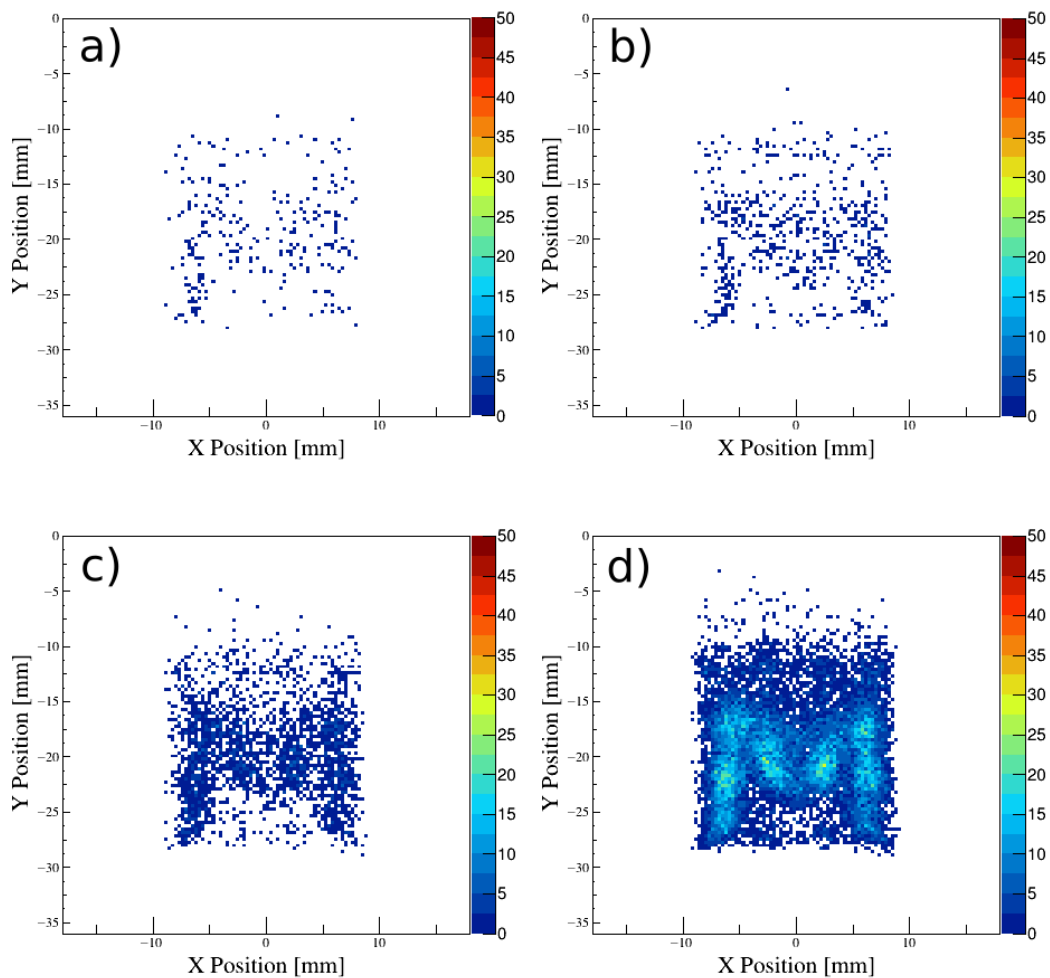
467 where (X_i, Y_i) and l_i are respectively the individual center position and detected light of each
 468 SiPM and L the light intensity detected during the event. The distribution of positions
 469 deduced for this approach can be plotted in a 2D image for which the pixel size can be
 470 reduced compared to the cell dimensions. For comparison purposes, it was chosen to reduce
 471 the size of the pixel by a factor 20, i.e. to a size of $300 \times 300 \mu\text{m}^2$. The result obtained using
 472 this algorithm is presented in Figure 9. Compared to the previous results, the M shape is
 473 clearly visible with this third algorithm proving the image reconstruction capability of the
 474 prototype.



475
 476
 477
 478

Figure 9 Spatial reconstruction of radioactive contamination of ^{14}C source after a M collimator using the weighted average algorithm

479 Finally, the effect of the acquisition duration on image reconstruction quality was studied by
480 performing measurements with 1, 5, 10 and 60 minutes durations. The results, obtained using
481 the weighted average algorithm, are represented in Figure 10. The study clearly shows that the
482 M shape is not visible after 1 minute, barely appears after 5 minutes but becomes clearly
483 visible after 10 minutes acquisition. These results are a huge progress compared to the
484 existing autoradiography methods which were used previously in dismantlement [12, 13, 14]
485 and for which the phosphor screens were typically exposed to radioactivity for several hours
486 or days.



487
488 **Figure 10** Spatial reconstruction of radioactive contamination of ^{14}C source after a M
489 collimator with the Weighted average algorithm. The four panels correspond to different
490 acquisition time: a) 1 minute, b) 5 minutes c) 10 minutes and d) 60 minutes.

491

492 5.3 Image reconstruction: discussion

493

494 Overall, the two tested algorithms have clearly shown the capability of the prototype to
495 distinguish spatial variations of contamination. In the case of the triggering cell algorithm,
496 image reconstructed is rather crude and a clear view of the collimator shape could not be
497 distinguished due to the intrinsic pixel resolution. Yet, this resolution is already suitable for
498 most cases encountered in dismantling applications where usually several hundreds of square
499 meters are investigated and a precision at the scale of the centimeter is acceptable. Besides,
500 this algorithm already provide a valuable first information if performed in real time and can
501 guide the user on the field. The weighted average algorithm clearly improves the
502 reconstruction of the M shape of the collimator but requires further data processing. The study
503 of the image reconstruction as a function of the acquisition time has shown that even at
504 relatively low level of activity (43 Bq total activity and 84 Bq/cm² surface activity of ¹⁴C)
505 about 5 to 10 minutes of acquisition is enough to provide a first image of the contamination.
506 Finally, if the two algorithms used in this work are enough to investigate image reconstruction
507 capability of the prototype, literature is widely available for pixel-based detectors (see for
508 example [28, 29]). Therefore, if required by the application, further improvements can be
509 foreseen with the prototype.

510

511 **7 Development of an industrial demonstrator**

512

513 Based on the experience gathered with the laboratory prototype, a first industrial demonstrator
514 was developed in collaboration with the Laumonier company². The demonstrator is designed
515 with a larger sensitive area, using four Hamamatsu S13361-6050, for a final spatial detection
516 of 5x5 cm² (see Figure 11). A new electronic, based on the same ASIC and FPGA as the initial
517 prototype, is designed to handle the readout of the 64 channels simultaneously. Specific
518 plastic scintillators, squared 5.5x5.5 cm² and 3 mm thick, were used to fully cover all the
519 sensitive surface of the SiPM arrays. The demonstrator is mainly developed to analyze
520 samples coming from facilities undergoing dismantling but also to perform measurements
521 directly on-site (for example on walls or floors). As a consequence, the device is designed to
522 be portable and with a power battery to provide autonomy in the field. A dedicated software
523 has been developed by the Laumonier company to perform online setup, operation, and image

²Ateliers Laumonier :. <https://www.at-laumonier.fr/>

524 reconstruction directly on the field. Finally, to insure a proper light insulation during the
525 measurement a specific rubber ring is designed to be place under the demonstrator cover.
526 Optimization of the software, handling and light shielding is still ongoing at the Laumonier
527 company but preliminary tests were performed in laboratory.



528

529

Figure 11 First demonstrator developed in collaboration with
the Laumonier company.

530

531

532 Investigation of the demonstrator image reconstruction is performed with two samples:

533

- A core sample from concrete contaminated on surface by ^{238}U (depleted Uranium).
534 Beforehand, the sample activity was estimated using standard alpha spectrometry. The
535 spatial contamination was estimated to be around 0.8 Bq/cm^2 for a total activity of 5
536 Bq.

537

- A tungsten sample which was prepared during the TRANSAT project [30]. The sample
538 is contaminated by tritium gas and its activity was estimated around 200 MBq on the
539 whole surface of the sample. This value is determined after a destructive measurement
540 of the sample after demonstrator measurements. The stability of the sample
541 contamination was controlled in laboratory before measurements.

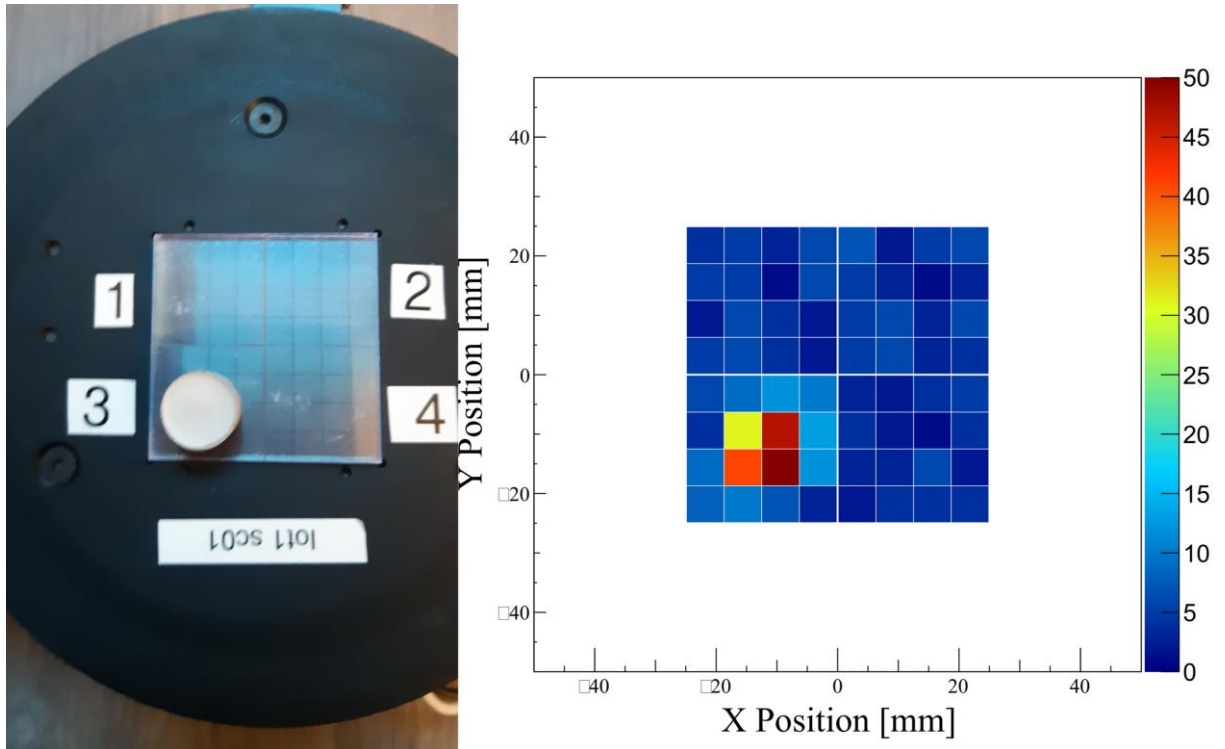
542

Contrary to the prototype, for which calibrated sources were used, it was chosen to test the
543 demonstrator with field type sample in order to have measurement conditions similar to
544 industrial applications.

545

For both samples, several measurements are performed with the demonstrator during a three
546 minutes acquisitions and using a 55 V bias voltage on the SiPM arrays (similar to the voltage

547 used with the laboratory). The measurements are undertaken in the same laboratory as the
548 prototype with similar temperature and humidity conditions. For each measurement, a
549 *triggering cell algorithm* is used to reconstruct the demonstrator contamination image. In both
550 cases the detection threshold was tuned to increase the image contrast.



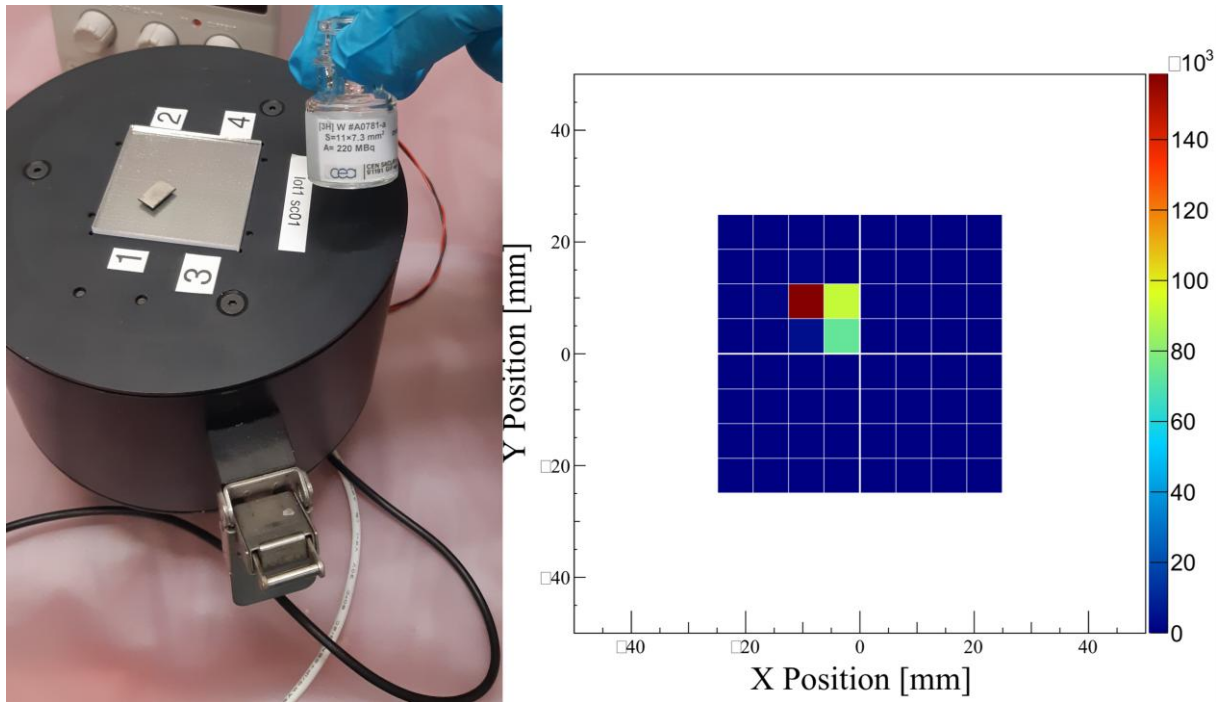
551

552 **Figure 12** Measurement with the industrial demonstrator of a concrete core sample
553 contaminated with Uranium

554 Regarding the concrete sample, the demonstrator was able to reconstruct properly the position
555 of the sample (example displayed in Figure 12). Given the low contamination of the sample,
556 this preliminary result is very promising for various facilities undergoing dismantlement in
557 France which require alpha contamination mapping.

558 Similarly, encouraging results are obtained with the tungsten sample. The image of the sample
559 could be reconstructed for several positions (example displayed in Figure 13). Contrary to the
560 previous concrete sample, mostly one single cell was triggering the acquisition. This could be
561 easily explained by the geometrical shape of the sample and the very short range of the tritium
562 radiation. Detecting tritium contamination with a portable device is always a challenge and
563 these preliminary results are thus very encouraging for the development of the demonstrator.

564 As a comparison, several acquisitions are also performed also without the use of any
565 radioactive source. For each of this background acquisition, the reconstructed image was
566 homogenous with very low count rate on each of the SiPM cells. .



567

568 **Figure 13** Measurement of a concrete core sample contaminated with the industrial
569 demonstrator

570 The demonstrator is currently being tested directly in various facilities in France. The
571 experience gathered in laboratory and in the field should provide very valuable data for the
572 development of an industrial contamination detector.

573

574 **8 Conclusion**

575 The preliminary development of an alpha / beta camera for dismantling applications has been
576 performed. A first prototype has been constructed with 32 SiPM cells of 6x6 mm² coupled to
577 organic scintillators and associated with an electronic readout based on a dedicated ASIC. The
578 prototype has been tested with alpha and beta sources commonly encountered in
579 dismantlement and has shown promising detection results: good beta and alpha detection
580 efficiency, direct tritium detection, relevant Minimum Detectable Activity for common
581 radioisotopes, linear response with activity and crude radiation discriminations. Additionally,
582 the image reconstruction performed with various algorithms has confirmed the position
583 sensitivity of the prototype within a reasonable acquisition time.

584 An industrial demonstrator, with an improved sensitive area ($5 \times 5 \text{cm}^2$), was designed and
585 constructed in collaboration with a French company based on the laboratory prototype first
586 results. The preliminary analyses performed with the demonstrator validate the capability of
587 the technology. With additional development and refinement the development could lead to
588 commercialization of alpha / beta detector for dismantling applications.

589

590 **Acknowledgments**

591 This work was performed within the Investments for the future program of the French
592 Government and operated by the French National Radioactive Waste Management Agency
593 (Andra). The authors want to acknowledge the support provided by WeeRoc company
594 regarding the operation of the dedicated ASIC. Finally, S. Leblond would like to express his
595 gratitude to C. Querré and N. Aychet for the technical support in the collimators design.

596

597 **References**

598 [1] International Atomic Energy Agency (2017) Radiological Characterization from a Waste
599 and Materials End-State Perspective: Practices and Experience, OECD

600

601 [2] Pérot B et al. (2018), The characterization of radioactive waste: a critical review of
602 techniques implemented or under development at CEA France, European Physical Journal
603 Nuclear Sciences & Technologies, 4: 1-24

604

605 [3] International Atomic Energy Agency (2013) Radiological characterization for
606 Decommissioning of Nuclear Installation, OECD

607

608 [4] International Atomic Energy Agency (2017) In Situ Analytical Characterization of
609 Contaminated Sites Using Nuclear Spectrometry Techniques, Analytical Quality in Nuclear
610 Applications Series 49

611

612 [5] Iltis A et al. (2018) Temporal Imaging CeBr 3 Compton Camera: A New Concept for
613 Nuclear Decommissioning and Nuclear Waste Management, European Physical Journal Web
614 of Conferences, 170: 1-5

615

616 [6] Sato Y et al. (2018) Remote radiation imaging system using a compact gamma-ray imager
617 mounted on a multicopter drone, Journal of Nuclear Science and Technology, 55: 90-96

618

- 619 [7] Amoyal G. et al. (2020) Development of a hybrid gamma camera based on Timepix3 for
620 nuclear industry applications, Nuclear Instruments and Methods in Physics Research Section
621 A: Accelerators, Spectrometers, Detectors and Associated Equipment, 9: 164838
622
- 623 [8] Pang X et al. (2019) A compact MPPC-based camera for omnidirectional (4π) fast-neutron
624 imaging based on double neutron-proton elastic scattering, Nuclear Instruments and Methods
625 in Physics Research Section A: Accelerators, Spectrometers, Detectors and Associated
626 Equipment, 944: 162471
627
- 628 [9] Kamiya Y et al. (2020) Development of a neutron imaging sensor using INTPIX4-SOI
629 pixelated, Nuclear Instruments and Methods in Physics Research Section A: Accelerators,
630 Spectrometers, Detectors and Associated Equipment, 979: 164400
631
- 632 [10] International Atomic Energy Agency (2014) R&D and Innovation Needs for
633 Decommissioning Nuclear Facilities, OECD
634
- 635 [11] Bergeret M J al. (2005) ESTAR, PSTAR, and ASTAR: Computer Programs for
636 Calculating Stopping-Power and Range Tables for Electrons, Protons, and Helium Ions, NIST
637 Standard Reference Database 124
638
- 639 [12] Fichet P et al. (2012), Tritium analysis in building dismantling process using digital
640 autoradiography, Journal of Radioanalytical Nuclear Chemistry, 291: 869–875
641
- 642 [13] Leskinen A et al. (2013) Digital autoradiography (DA) in quantification of trace level
643 beta emitters on concrete, Journal of Radioanalytical Nuclear Chemistry, 298:153–161
644
- 645 [14] Haudebourg R et al. (2015) A non-destructive and on-site digital autoradiography-based
646 tool to identify contaminating radionuclide in nuclear wastes and facilities to be dismantled,
647 Journal of Radioanalytical Nuclear Chemistry, 309: 551–561
648
- 649 [15] Morishita Y et al. (2017) Flexible alpha camera for detecting plutonium contamination,
650 Radiation Measurements, 103: 33-38
651
- 652 [16] Kim J et al. (2018) Feasibility of miniature radiation portal monitor for measurement of
653 radioactivity contamination in flowing water in pipe, Journal of Instrumentation, 13: 1022-
654 1022
655
- 656 [17] Morishita Y et al. (2017) Flexible alpha camera for detecting plutonium contamination,
657 Radiation Measurements, 103: 33-38

658

659 [18] L'Annunziata M (2020) Handbook of Radioactivity Analysis Volume 1: Radiation
660 Physics and Detectors, 4th ed, Academic Press

661

662 [19] Klanner R (2019) Characterisation of SiPMs, Nuclear Instruments and Methods in
663 Physics Research Section A: Accelerators, Spectrometers, Detectors and Associated
664 Equipment, 926 36-56

665

666 [20] Billon S et al. (2019) From Bq cm⁻³ to Bq cm⁻² (and conversely)—part 1: a useful
667 conversion for autoradiography, Journal of Radioanalytical Nuclear Chemistry, 320: 643–654

668

669 [21] Billon S et al. (2019) From Bq cm⁻³ to Bq cm⁻² (and conversely)—part 2: useful
670 dataset to apply the conversion to decommissioning operations, Journal of Radioanalytical
671 Nuclear Chemistry, 320: 699–709

672

673 [22] Walpole R E et al. (2006) Probability & Statistics for Engineers & Scientists, 7th ed,
674 John Wiley & Sons Inc, Pearson

675

676 [23] Kirkpatrick J M et al. (2013) Minimum detectable activity, systematic uncertainties, and
677 the ISO 11929 standard, Journal of Radioanalytical Nuclear Chemistry, 296: 1005-1010

678

679 [24] Knoll G, Radiation Detection and Measurement, 4th edition (2010) John Wiley & Sons
680 Inc, Verlag

681

682 [25] Berthold, LB 124 SINCT contamination monitor, available at
683 [https://www.berthold.com/en/radiation-protection/products/contamination-monitors/alpha-](https://www.berthold.com/en/radiation-protection/products/contamination-monitors/alpha-beta-gamma-measurement-lb-124-scint/)
684 [beta-gamma-measurement-lb-124-scint/](https://www.berthold.com/en/radiation-protection/products/contamination-monitors/alpha-beta-gamma-measurement-lb-124-scint/) Accessed on June 18th, 2021

685

686 [26] *NUVIATECH Instruments*, Specification sheet CoMo-170/300, available at
687 <http://www.nuviatech-healthcare.com/product/hand-held-contamination-monitor/> Accessed on
688 June 18th, 2021

689

690 [27] *United Nations Economic Commission for Europe*, International Carriage of Dangerous
691 Goods by Road, Volume I: Agreement and Protocol of Signature 2019 ed, available at
692 http://www.unece.org/trans/danger/publi/adr/adr_f.html Accessed on June 18th, 2021

693

694 [28] Esposito M et al. (2011) Energy sensitive Timepix silicon detector for electron imaging,
695 Nuclear Instruments and Methods in Physics Research Section A: Accelerators,
696 Spectrometers, Detectors and Associated Equipment, 652: 458-461

697

698 [29] Gehrke T et al (2018) Theoretical and experimental comparison of proton and helium-
699 beam radiography using silicon pixel detectors, Physics in Medicine & Biology, 63: 035037

700

701 [30] Bernard E et al (2019) Tritium retention in W plasma-facing materials: Impact of the
702 material structure and helium irradiation, Nuclear Materials and Energy, 19: 403-410